Chemical Science

ROYAL SOCIETY OF CHEMISTRY

EDGE ARTICLE

View Article Online
View Journal | View Issue

Cite this: *Chem. Sci.*, 2023, **14**, 12283

All publication charges for this article have been paid for by the Royal Society of Chemistry

The role of metal accessibility on carbon dioxide electroreduction in atomically precise nanoclusters†

Yingwei Li, ‡ Grant J. Stec, ‡ Agnes E. Thorarinsdottir, Ryan D. McGillicuddy, Shao-Liang Zheng and Jarad A. Mason *

Received 5th August 2023
Accepted 9th October 2023

DOI: 10.1039/d3sc04085b

rsc.li/chemical-science

Atomically precise nanoclusters (NCs) can be designed with high faradaic efficiency for the electrochemical reduction of CO_2 to CO (FE_{CO}) and provide useful model systems for studying the metal-catalysed CO_2 reduction reaction (CO_2RR). While size-dependent trends are commonly evoked, the effect of NC size on catalytic activity is often convoluted by other factors such as changes to surface structure, ligand density, and electronic structure, which makes it challenging to establish rigorous structure–property relationships. Herein, we report a detailed investigation of a series of NCs [$Au_nAg_{46-n}(C{\equiv}CR)_{24}Cl_4(PPh_3)_2$, $Au_{24}Ag_{20}(C{\equiv}CR)_{24}Cl_2$, and $Au_{43}(C{\equiv}CR)_{20}/Au_{42}Ag_1(C{\equiv}CR)_{20}$] with similar sizes and core structures but different ligand packing densities to investigate how the number of accessible metal sites impacts CO_2RR activity and selectivity. We develop a simple method to determine the number of CO_2-accessible sites for a given NC then use this to probe relationships between surface accessibility and CO_2RR performance for atomically precise NC catalysts. Specifically, the NCs with the highest number of accessible metal sites [$Au_{43}(C{\equiv}CR)_{20}$ and $Au_{42}Ag_1(C{\equiv}CR)_{20}$] feature a FE_{CO} of >90% at −0.57 V *vs.* the reversible hydrogen electrode (RHE), while NCs with lower numbers of accessible metal sites have a reduced FE_{CO}. In addition, CO_2RR studies performed on other Au–alkynyl NCs that span a wider range of sizes further support the relationship between FE_{CO} and the number of accessible metal sites, regardless of NC size. This work establishes a generalizable approach to evaluating the potential of atomically precise NCs for electrocatalysis.

Introduction

Heterogeneous catalysts composed of metal nanoparticles (NPs) dispersed on high-surface-area supports have been studied for more than a century,[1–3] and these catalysts are of increasing interest for the electrochemical reduction of CO_2 into chemical fuels and feedstocks.[4–6] Gold- and silver-based NPs are particularly effective for the selective reduction of CO_2 to CO.[7] Though the effects of nanoparticle size,[8–10] shape,[11,12] and surface ligands[13,14] on the CO_2 reduction reaction (CO_2RR) have been widely studied, the nonuniformity of metal NP catalysts is a long-standing challenge in the investigation of fundamental catalytic mechanisms.[1,15] In particular, it is often difficult to identify the specific active sites that drive catalysis because of the wide distribution of local microenvironments in ligand-protected NPs that adopt varying sizes, shapes, and surface structures.[16,17] For example, although functionalization with larger organic ligands has been shown to enhance the CO_2RR activity of Au NPs,[18,19] uncertainty over the exact arrangement of surface ligands makes it difficult to determine how bulky ligands impact selectivity and catalytic activity. Such molecular-level insight is, however, possible when atomically precise nanoclusters (NCs) are used as catalysts, since their uniformity allows the entire particle structure—including the ligand shell—to be resolved crystallographically.[20–23]

Soon after the canonical $Au_{25}(SR)_{18}$ (SR = aryl or alkylthiolate) NC was first reported, it was shown to be effective for CO_2RR, featuring a high faradaic efficiency for CO (FE_{CO}) at –1 V *vs.* the reversible hydrogen electrode (RHE).[24] Though the CO_2RR has since been studied for many other atomically precise Au NCs,[25–28] there still remains much to be understood about how NC size, structure, and surface ligand identity influence catalytic activity and selectivity. For instance, relationships between NC size and CO_2RR activity are challenging to identify because the ligand-to-metal ratio typically increases for smaller NCs,[29–31] resulting in higher surface coverage. Changes to the arrangement of surface ligands and metal atoms—as well as the electronic structure of the NC—may also affect the outcome of catalytic reactions, further convoluting

Department of Chemistry & Chemical Biology, Harvard University, 12 Oxford Street, Cambridge, Massachusetts, 02138, USA. E-mail: mason@chemistry.harvard.edu

† Electronic supplementary information (ESI) available. CCDC 2260158 and 2260159. For ESI and crystallographic data in CIF or other electronic format see DOI: https://doi.org/10.1039/d3sc04085b

‡ These authors contributed equally to this work.

structure–property relationships.[32] Indeed, differing trends have been reported for how NC size affects CO_2RR activity. For example, in the series $Au_{25}(SR)_{18}$, $Au_{38}(SR)_{24}$, and $Au_{144}(SR)_{60}$ (SR = SC_2H_4Ph), CO_2RR activity increases with increasing NC size,[33] while other studies have found that the FE_{CO} of Au-SR NCs is not directly affected by NC size.[34] Given the different size-dependent trends that have been observed for atomically precise NCs, the number of active sites is often a better predictor of catalytic behavior but is difficult to manipulate in a predictable fashion.

In an effort to decouple the role of metal active sites from NC size, structure, and ligand type, we designed a series of alkynyl-protected atomically precise Au/Ag NCs with similar sizes and core structures but different degrees of surface ligand coverage. We investigated the CO_2RR performance of these NCs and developed a convenient computational method to quantitatively evaluate the accessibility of potential catalytically active sites. Critically, the use of acetylene-based ligands—bearing one rotatable bond—simplifies the conformational landscape at the metal–ligand interface, thereby clarifying the effect of ligand modification on surface coverage and the number of accessible metal sites. In particular, we found that the number and accessibility of surface metal sites is directly correlated to experimental CO_2RR activity.

Results and discussion

Synthesis and characterization of alkynyl-protected Au/Ag NCs

We recently reported the isostructural alkynyl-protected NCs $Au_{43}(C{\equiv}C^tBu)_{20}$ (**Au_{43}**) and $Au_{42}Ag_1(C{\equiv}C^tBu)_{20}$ (**$Au_{42}Ag_1$**), which are synthesized by reducing an oligomeric Au^I–C≡C^{t}Bu or Au^I/Ag^I–C≡C^{t}Bu precursor with borane *tert*-butylamine then purifying *via* thin layer chromatography (Fig. S1A†).[35] With a nearly identical NC core but an increased density of alkynyl surface ligands, we also selected the previously reported $Au_{24}Ag_{20}(C{\equiv}CPh^tBu)_{24}Cl_2$ NC (**$Au_{24}Ag_{20}$**) for comparison (Fig. S1B†).[36,37] To complete a series of NCs with similar sizes and varying surface ligand densities, we also targeted an Au/Ag–alkynyl NC with an even denser organic shell. This was achieved by introducing a bulky triphenylphosphine (PPh_3) ligand through the "hydride-mediated conversion" method.[38,39] Specifically, $[Au_9(PPh_3)_8]^{3+}$ (ref. 40) was reduced with $NaBH_4$ to furnish a hydride-doped $[HAu_9(PPh_3)_8]^{2+}$ cluster, which was then reacted with CH_3COOAg, *meta*-substituted phenylacetylene ligands, and triethylamine to yield NCs with a composition of $Au_nAg_{46-n}(C{\equiv}CPh{-}m{-}X)_{24}Cl_4(PPh_3)_2$ (**Au_nAg_{46-n}**, n = 16–19, X = H, F, CH_3) (Fig. 1, see ESI† for experimental details). Though attempts to grow single crystals of $Au_nAg_{46-n}(C{\equiv}CPh)_{24}Cl_4(PPh_3)_2$ suitable for structure determination were unsuccessful, crystal structures were successfully determined for **Au_nAg_{46-n}** with X = F and CH_3 (see Fig. 2). The successful crystallization of **Au_nAg_{46-n}** with *meta*-substituted phenylacetylene ligands can be attributed to the additional interparticle C–H···π, or C–F···π interactions between the *meta* functional groups on one NC and the phenyl rings of ligands on another NC (Fig. S2 and S3†).[41,42]

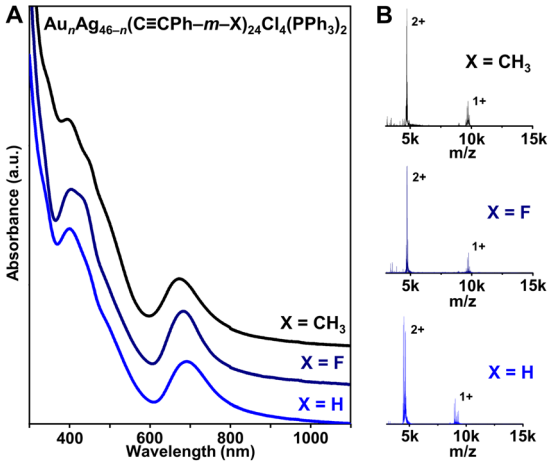

Fig. 1 (A) UV-vis-NIR absorption spectra and (B) ESI-MS of $Au_nAg_{46-n}(C{\equiv}CPh{-}m{-}X)_{24}Cl_4(PPh_3)_2$ (n = 16–19, X = H, F, or CH_3).

The solution-phase UV-vis absorption spectra of all three **Au_nAg_{46-n}** NCs with different protecting ligands exhibit sharp absorption peaks centered near 400 and 690 nm (Fig. 1A). Moreover, electrospray ionization mass spectrometry (ESI-MS) analysis shows 2+ and 1+ ion peaks for the NCs (Fig. 1B). Combined with the X-ray crystallography data, the 2+ and 1+ charges are attributed to ionization in ESI-MS—not the native charge states of the NCs—and the peaks correspond to NCs that have lost one or two PPh_3 ligands, which has been commonly observed for similar atomically precise NCs (Fig. S4–S6†).[43,44] The ESI-MS spectrum of $Au_nAg_{46-n}(C{\equiv}CPh{-}m{-}F)_{24}Cl_4(PPh_3)_2$ contains peaks corresponding to n = 16, 17, and 18 (Fig. S5†), consistent with the crystallographically refined composition of $Au_{17.67}Ag_{28.33}(C{\equiv}CPh{-}m{-}F)_{24}Cl_4(PPh_3)_2$ (Tables S1 and S2†). When HC≡CPh–m–CH_3 was used instead, three peaks corresponding to n = 17, 18, and 19 were found, which is consistent with the higher refined Au : Ag ratio in $Au_{19}Ag_{27}(C{\equiv}CPh{-}m{-}CH_3)_{24}Cl_4(PPh_3)_2$ (Tables S3 and S4†). The small inconsistency between MS and X-ray crystallography data has also been observed for other heterometallic NCs, which are known to be dynamic—and prone to rearrangement—in solution.[45,46] Regardless, the similar UV-vis and ESI-MS spectra for $Au_nAg_{46-n}(C{\equiv}CPh)_{24}Cl_4(PPh_3)_2$ and $Au_nAg_{46-n}(C{\equiv}CPh{-}m{-}X)_{24}Cl_4(PPh_3)_2$ (X = F, CH_3) NCs—along with the fact that the same synthesis conditions were used—suggest that the three NCs are isostructural. Note that small differences in absorption features near 400 nm and shifts in MS can be attributed to the different alkynyl ligands used.

The series of five atomically precise Au/Ag NCs exhibit similar core structures. Specifically, **Au_nAg_{46-n}** has an icosahedral Au_nAg_{12-n} kernel (n = 4–7 with Au and Ag randomly distributed), a dodecahedral Ag_{20} inner shell, and an icosahedral Au_{12} outer shell with two additional Ag atoms on the surface (Fig. 2A). Each of the additional Ag atoms on the surface of **Au_nAg_{46-n}** is bonded to two chloride ligands, one Au atom in the outer shell, and one PPh_3 ligand. Four chloride ligands are necessary for **Au_nAg_{46-n}** to adopt a closed-shell superatomic

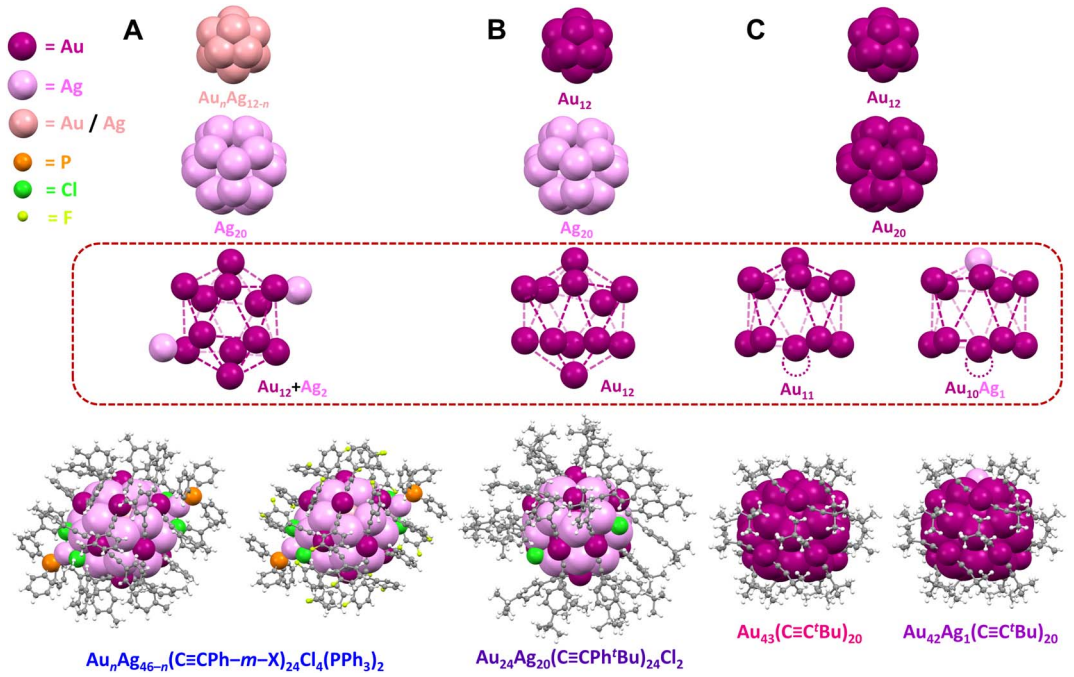

Fig. 2 Structures of (A) $Au_nAg_{46-n}(C{\equiv}CPh{-}m{-}X)_{24}Cl_4(PPh_3)_2$ ($n = 16$–19, X = F or CH_3), (B) $Au_{24}Ag_{20}(C{\equiv}CPh^tBu)_{24}Cl_2$, and (C) $Au_{43}(C{\equiv}C^tBu)_{20}$ and $Au_{42}Ag_1(C{\equiv}C^tBu)_{20}$, Color code: magenta = Au; violet = Ag; light pink = Au/Ag; orange = P; green = Cl; light green = F; grey = C; white = H. The vacant surface sites in $Au_{43}(C{\equiv}C^tBu)_{20}$ and $Au_{42}Ag_1(C{\equiv}C^tBu)_{20}$ are indicated with a dashed circle.

electronic configuration ($46 - 24 - 4 = 18$ e^-) similar to **$Au_{24}Ag_{20}$** with two chloride ligands ($24 + 20 - 24 - 2 = 18$ e^-). The structure of **$Au_{24}Ag_{20}$** also consists of an icosahedral Au_{12} kernel, a dodecahedral Ag_{20} inner shell, and an icosahedral Au_{12} outer shell (Fig. 2B), while **Au_{43}/$Au_{42}Ag_1$** has an icosahedral Au_{12} kernel, a dodecahedral Au_{20} inner shell, and an incomplete icosahedral Au_{11} or $Au_{10}Ag_1$ outer shell with a single vacant surface site (Fig. 2C).

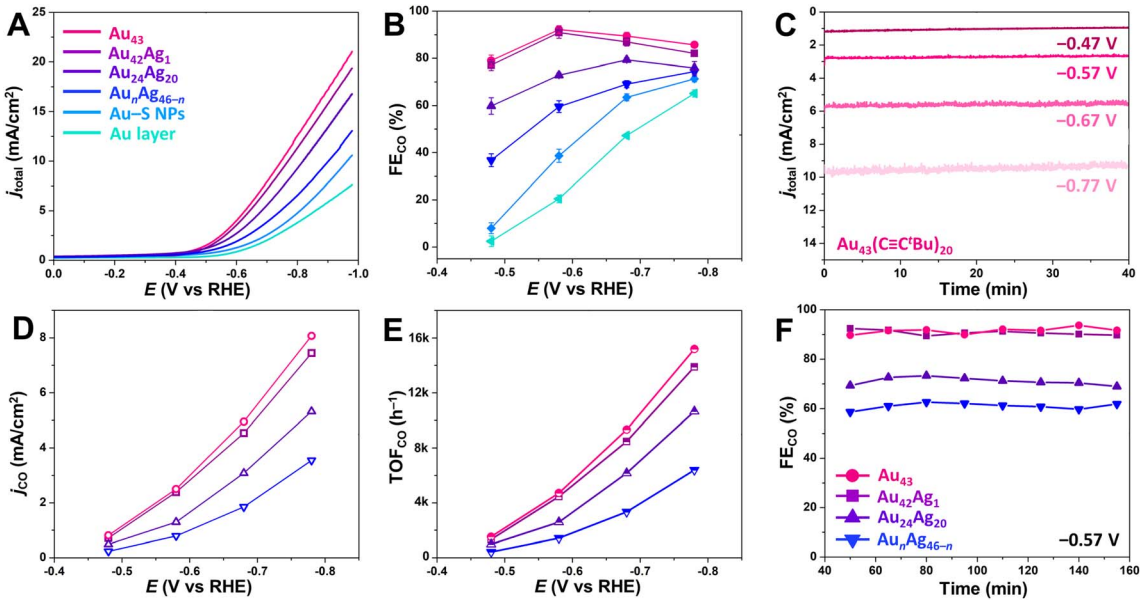

Fig. 3 (A) LSV and (B) FE_{CO} for CO_2RR for the series of NC-based catalysts. (C) Chronoamperometry data for the **Au_{43}**-based catalyst at different applied potentials. (D) j_{CO} and (E) TOF_{CO} for the NC-based catalysts at different applied potentials during CO_2RR. (F) FE_{CO} for the NC-based catalysts at −0.57 V *vs.* RHE during CO_2RR over an extended time period. All experiments were conducted in a 0.5 M $KHCO_3$ solution saturated with CO_2. In panels A, B, D, E, and F, magenta represents $Au_{43}(C{\equiv}C^tBu)_{20}$, purple represents $Au_{42}Ag_1(C{\equiv}C^tBu)_{20}$, indigo represents $Au_{24}Ag_{20}(C{\equiv}CPh^tBu)_{24}Cl_2$, blue represents $Au_nAg_{46-n}(C{\equiv}CPh)_{24}Cl_4(PPh_3)_2$, sky blue represents Au-SC_2H_4Ph NPs, and cyan represents the Au layer.

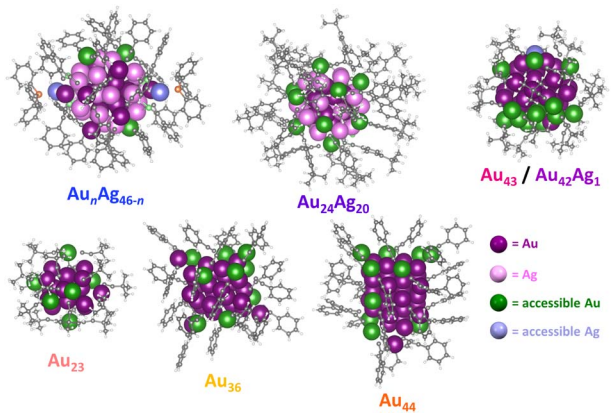

Fig. 4 The metal sites accessible to CO_2 on the surface of different Au/Ag-alkynyl NCs.

Adding or removing a single metal atom to or from the surface of NCs has provided insight into the optical and electronic properties of thiolate-capped metal NCs.[47,48] The successful synthesis of our series of NCs with the same core (M_{46}, M_{44}, and M_{43}; M = Au and/or Ag) represents—to the best of our knowledge— the first demonstration of atom-by-atom evolution for alkynyl-stabilized metal NCs structure (Fig. 2). Moreover, the linear directionality of alkynyl ligands in alkynyl-stabilized NCs offer advantages for catalytic studies since the NC/electrolyte interface is dominated by Au–C≡C bonds with similar local arrangements. Note that for $\mathbf{Au_nAg_{46-n}}$ and $\mathbf{Au_{24}Ag_{20}}$, Ag atoms are located in the inner dodecahedral Ag_{12} shell and/or the icosahedral Au_nAg_{12-n} kernel which are not accessible to substrates interacting with the surface of the NC (Fig. 2, highlighted by the dashed red box). Importantly, the surface ligand density varies systematically across the series: 24 alkynyl, 4 chloride, and 2 phosphine ligands for $\mathbf{Au_nAg_{46-n}}$, 24 alkynyl and 2 chloride ligands for $\mathbf{Au_{24}Ag_{20}}$, and only 20 alkynyl ligands for $\mathbf{Au_{43}}$ and $\mathbf{Au_{42}Ag_1}$. Thus, this series of atomically precise NCs provides a powerful platform to study relationships between metal site accessibility and CO_2RR activity.

Evaluation of CO_2RR activity and selectivity

To investigate their efficacy for CO_2RR catalysis, synthesized atomically precise NCs were mixed with carbon black (20 wt% NC loading) and deposited on a carbon paper electrode. For comparison, a carbon electrode was also prepared with spherical Au–SC_2H_4Ph NPs (**Au–S NPs**) with an average diameter of 3.1 ± 0.4 nm (Fig. S1C†) that were mixed with carbon black at the same mass loading. To provide an additional comparison, an 85 nm thick bulk gold layer was also deposited on one carbon paper electrode (referenced as **Au layer**) by electron beam deposition. Linear sweep voltammetry (LSV) was then performed for each electrode in CO_2-saturated 0.5 M $KHCO_3$ solution. For the atomically precise NCs, the current density (j_{total}) was found to increase in the order of $\mathbf{Au_nAg_{46-n}}$ < $\mathbf{Au_{24}Ag_{20}}$ < $\mathbf{Au_{42}Ag_1}$ < $\mathbf{Au_{43}}$ (Fig. 3A). Larger sized **Au–S NPs** exhibited a lower j_{total} than all atomically precise NCs, and j_{total} for the **Au layer** was the lowest of all catalysts investigated here (Fig. 3A). We note that the NC catalysts were not activated before electrocatalysis to minimize possible ligand stripping, and the LSV curves taken before and after chronoamperometric CO_2RR catalysis (potential range of −0.47 V to −0.77 V *vs.* RHE) were in close agreement (Fig. S7†). Moreover, the NC-based catalysts display a steady current density over at least 40 min at each applied voltage (−0.47 V, −0.57 V, −0.67 V and −0.77 V *vs.* RHE; Fig. 3C), and the absorption spectra of NCs recovered from the electrode after catalysis matched those of as-synthesized NCs (Fig. S8†), confirming the stability of the NCs during CO_2RR catalysis.

For all atomically precise NC catalysts evaluated here, CO was the major CO_2RR product, and H_2 was the sole byproduct with no liquid products detected by ^{1}H NMR spectroscopy. The faradaic efficiency for CO production (FE_{CO}) was assessed for each catalyst by calculating the percentage of transferred charge that was directed toward CO production (see ESI† for details), and the highest FE_{CO} were 92.1 ± 1.7% and 90.9 ± 1.4% for $\mathbf{Au_{43}}$ and $\mathbf{Au_{42}Ag_1}$, respectively, at a potential of −0.57 *vs.* RHE (Fig. 3B). At the same potential, FE_{CO} for $\mathbf{Au_{24}Ag_{20}}$ and $\mathbf{Au_nAg_{46-n}}$ were just 72.9 ± 1.0% and 59.5 ± 2.5%, respectively (Fig. 3B). These lower efficiencies can be attributed to more densely packed surface ligands, which likely favors the hydrogen evolution reaction (HER) over CO_2RR.[25,26,49] The **Au–S NPs** have an even lower FE_{CO} (38.7 ± 0.8%) at the same potential, which is consistent with previously reported studies.[27,33] If FE_{CO} is related to the density of surface ligands, one might assume that a ligand-free **Au layer** would have the

Table 1 The calculated number of accessible metal sites (*N*) for a series of alkynyl-protected NCs, along with their experimentally determined FE_{CO}, j_{CO}, TOF_{CO}, and TOF_{CO}/N values for CO_2RR electrocatalysis at −0.57 V *vs.* RHE. All experiments were conducted in a 0.5 M $KHCO_3$ solution saturated with CO_2

Catalyst	Number of accessible metals (*N*)	FE_{CO} (%)	j_{CO} (mA cm^{-2})	TOF_{CO} (h^{-1})	TOF_{CO}/N (h^{-1})
Au_{43}	16	92.1 ± 1.7	2.5	4718	295
$Au_{42}Ag_1$	16	90.9 ± 1.4	2.4	4458	279
$Au_{24}Ag_{20}$	12	72.9 ± 1.0	1.3	2597	216
Au_nAg_{46-n}	5	59.5 ± 2.5	0.8	1427	285
Au_{44}	12	74.5 ± 1.3	1.0	2045	170
Au_{36}	9	69.7 ± 1.6	0.7	1325	147
Au_{23}	6	66.7 ± 2.5	0.7	794	132

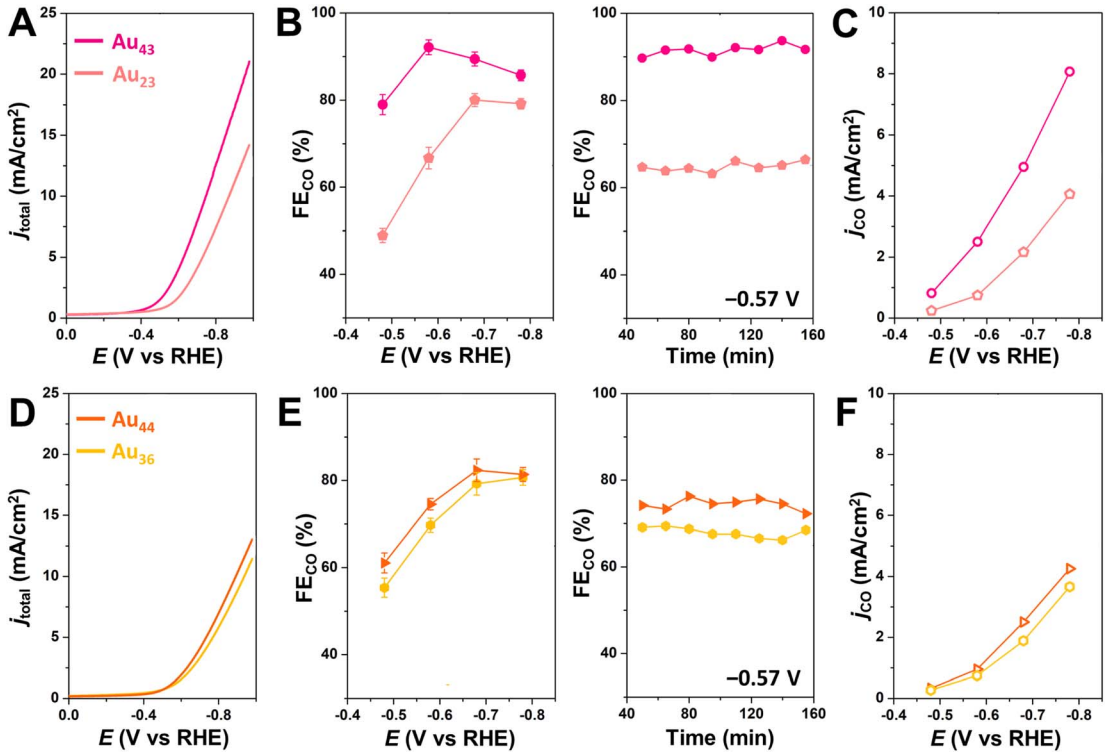

Fig. 5 (A/D) LSV, (B/E) FE_{CO} at different applied potentials (left), or at −0.57 V *vs.* RHE for prolonged time (right), and (C/F) j_{CO} at different applied potentials during CO_2RR for NC-based catalysts conducted in CO_2-saturated 0.5 M $KHCO_3$ solution. Magenta represents $Au_{43}(C{\equiv}C^tBu)_{20}$, pink represents $Au_{23}(C{\equiv}C^tBu)_{20}$, orange represents $Au_{44}(C{\equiv}CPh)_{28}$, and yellow represents $Au_{36}(C{\equiv}CPh)_{24}$.

highest efficiency. However, the FE_{CO} for the **Au layers** is only 20.4 ± 1.6% at −0.57 V *vs.* RHE, highlighting the important role of the microenvironments created by nanostructured catalysts in driving CO_2RR.[3,50,51]

To further evaluate catalytic performance, CO partial current densities (j_{CO}) were determined and compared across the NC series. Generally, j_{CO} decreases with increasing ligand density on the surface (Fig. 3D): $\mathbf{Au_{43}/Ag_{42}Ag_1}$ (20 surface ligands) > $\mathbf{Au_{24}Ag_{20}}$ (26 surface ligands) > $\mathbf{Au_nAg_{46-n}}$ (30 surface ligands). For $\mathbf{Au_{43}}$, j_{CO} is slightly higher than for $\mathbf{Au_{42}Ag_1}$, suggesting that substitution of a single surface Au atom for Ag leads to a small decrease in CO_2RR performance, particularly at more negative potentials. Furthermore, $\mathbf{Au_{43}}$ shows a high CO turnover frequency (TOF_{CO}) of 4718 h^{-1} at −0.57 V and 15 193 h^{-1} at −0.77 V *vs.* RHE (Fig. 3E), which exceeds the values for $\mathbf{Au_{24}Ag_{20}}$ (2597 h^{-1} at −0.57 V and 10 658 h^{-1} at −0.77 V) and $\mathbf{Au_nAg_{46-n}}$ (1427 h^{-1} at −0.57 V and 6400 h^{-1} at −0.77 V). Note that the same mass loading of NCs was used for all experiments. This makes it reasonable to directly compare TOF values since the NCs in this series have similar molecular weights (Table S5†). In addition, differences in catalytic activity cannot be attributed to differences in NC stability as the FE_{CO} of all catalysts remained constant for at least 2.5 hours at −0.57 V (Fig. 3F).

While the nature of active sites is regarded as one of the best predictors of catalytic activity,[52] it is often challenging to experimentally determine the number of catalytically active sites in a nanostructured material, and theoretical models are required.[53,54] Though double-layer capacitance measurements can be used to determine the electrochemically active surface area (ECSA) of catalysts, the ECSA might not reflect the surface area active specifically for CO_2RR since CO_2RR and HER frequently occur simultaneously. For example, previous studies have shown that $Au_{25}(SR)_{18}$ and $Au_{38}(SR)_{24}$ exhibit different CO_2RR behavior even though the NCs have almost the same ECSA.[33,49] The ligand-to-metal ratio can serve as a proxy for active site density when the sizes of NCs are similar,[55] but this ratio is not directly related to the number of active sites owing to the different shapes and surface structures that similarly sized NCs can adopt. Indeed, two isomeric $Au_{38}(SR)_{24}$ NCs with the same ligand-to-metal ratio have shown significant differences in CO_2RR catalysis.[34]

With these challenges in mind, we sought to establish a simple method for determining the number of metal sites accessible to CO_2 in atomically precise NCs that does not rely on computationally intensive density functional theory (DFT) calculations. Briefly, the NC structure determined by crystallography is used to generate a series of several thousand conformers accounting for the different ligand conformations that may arise due to ligand rotation in the absence of crystal packing effects (see ESI† for details). The accessible surface area of each conformation within the conformer series was then calculated for every surface atom using a 1.65 Å spherical probe (the kinetic radius of CO_2, Fig. S9†).[56] Metal atoms with a positive contact area with CO_2 (Fig. S10†) were counted as accessible since these atoms have sufficient space to accommodate a covalent bond with CO_2. Accessible metal atoms for the

different alkynyl-protected NCs under investigation are highlighted in Fig. 4. Note that the NC conformation with the greatest number of accessible metal atoms (N) was used to represent the surface accessibility of each NC. Using this approach, the number of accessible metal atoms for each NC can be calculated in ~1 hour. Notably, the number of accessible metal atoms, N, for $\mathbf{Au_{43}}$/$\mathbf{Au_{42}Ag_1}$, $\mathbf{Au_{24}Ag_{20}}$, and $\mathbf{Au_nAg_{46-n}}$ are 16, 12, and 5, respectively, which is consistent with a greater density of CO_2-accessible surface metal sites driving increased CO_2RR activity. The role of CO_2-accessible metal sites is further supported by the fact that we observe little variation in TOF_{CO} when it is normalized to the number of accessible metal sites on each NC (TOF_{CO}/N). Specifically, TOF_{CO}/N for $\mathbf{Au_{43}}$, $\mathbf{Au_{42}Ag_1}$, $\mathbf{Au_{24}Ag_{20}}$, and $\mathbf{Au_nAg_{46-n}}$ is 294 h^{-1}, 279 h^{-1}, 216 h^{-1} and 285 h^{-1}, respectively, at –0.57 V *vs.* RHE (Table 1 and Fig. S11†). This suggests that the number of CO_2-accessible metal sites—rather than the degree of Ag doping,[57] surface ligand functional groups,[58] or the electronic structure[59] of the cluster—is the primary driver of catalytic activity, at least for NCs with relatively similar structures and compositions.

To further investigate the generalizability of accessible metal site number as a predictor of CO_2RR activity, we also evaluated a wider range of previously reported alkynyl-protected Au NCs: $Au_{23}(C{\equiv}C^tBu)_{15}$ ($\mathbf{Au_{23}}$),[60] $Au_{36}(C{\equiv}CPh)_{24}$ ($\mathbf{Au_{36}}$), and $Au_{44}(C{\equiv}CPh)_{28}$ ($\mathbf{Au_{44}}$)[61] (Fig. S12†). Within this series, $\mathbf{Au_{44}}$ has the highest number of CO_2-accessible metal sites ($N = 12$) and the highest CO_2RR activity, while $\mathbf{Au_{23}}$ has the lowest number of CO_2-accessible sites and the lowest CO_2RR activity (Fig. 5). The activity of $\mathbf{Au_{44}}$, however, is much lower than that of $\mathbf{Au_{43}}$, which is consistent with the greater number of CO_2-accessible metal sites ($N = 16$) for the latter NC (Table 1 and Fig. S13†). The relationship between the number of accessible metal sites and FE_{CO}, j_{CO} is plotted in Fig. S14.† This highlights that even though larger sized Au–alkynyl NCs often have increased CO_2RR activities, just like their Au–thiolate counterparts,[33] the number of accessible surface metals tends to be more closely related to catalyst performance. Therefore, we conclude that the number of accessible metal sites provides a useful metric for evaluating the likelihood of CO_2 binding to a particular atomically precise NC and for predicting trends in catalytic activity. Since $\mathbf{Au_{43}}$ and $\mathbf{Au_{42}Ag_1}$ NCs are isostructural, their slight difference in CO_2RR activity could be due to replacing a surface Au atom with a more electropositive Ag atom.[35] Though $\mathbf{Au_{24}Ag_{20}}$ and $\mathbf{Au_{44}}$ NCs have the same number of metal atoms (44) as well as the number of accessible metals (12), $\mathbf{Au_{44}}$ exhibits a slightly higher FE_{CO} and lower j_{CO} than $\mathbf{Au_{24}Ag_{20}}$. Differences in the geometric and electronic structures of the NCs may influence their CO_2RR performance, but this is likely a less significant effect than the number of accessible metals. For NCs of the same core structure, more valence electrons in the frontier molecular orbitals elevate the energy of the highest occupied molecular orbital (HOMO), thereby favoring electron transfer from the NC catalyst to the substrate and thus improving the CO_2RR activity.[59] The performance of $\mathbf{Au_{43}}$ and $\mathbf{Au_{42}Ag_1}$ NCs could also be partially attributed to more facile electron transfer during electrocatalysis. However, since the electronic structure of the NCs is determined by the number of metals and ligands, the surface coverage is still of importance. Moreover, since calculating the number of accessible metal sites is straightforward, it can serve as a quick screening tool for identifying the most promising NCs for electrochemical catalysis that is complementary to advanced DFT calculations.

Conclusions

A series of alkynyl-stabilized NCs with similar sizes and core structures but different degrees of surface ligand coverage was used to provide insight into the effect of the number of accessible metal sites on electrochemical CO_2RR activity. A simple computational method was developed to calculate the number of metal sites on the NCs that are accessible to CO_2. The highest faradaic efficiencies for CO_2RR were observed for $\mathbf{Au_{43}}$ and $\mathbf{Au_{42}Ag_1}$, which feature the largest number of accessible metal sites. When the TOF_{CO} of the NC-based catalysts was normalized by the number of accessible sites, the differences between NCs were reduced. Collectively, these trends suggest that the number of substrate-accessible metal sites serves as a useful and generalizable predictor for evaluating the potential of atomically precise NCs for CO_2RR.

Data availability

All the data are shown in the manuscript or the associated ESI.†

Author contributions

J. A. M and Y. L. conceived the project. Y. L. synthesized the NCs and grew the single crystals. Y. L. and A. E. T. performed the electrochemical studies and analysed the data. G. J. S performed the computational studies. R. D. M. and S.-L. Z. solved the crystal structures. Y. L and G. J. S wrote the manuscript with contribution from other authors.

Conflicts of interest

There are no conflicts to declare.

Acknowledgements

We acknowledge support from the Major Research Instrumentation (MRI) Program of the National Science Foundation under NSF award no. 2216066 for the X-ray facility. This research was partially supported by the Arnold and Mabel Beckman Foundation through a Beckman Young Investigator grant awarded to J. A. M.

References

1 L. Liu and A. Corma, Metal Catalysts for Heterogeneous Catalysis: From Single Atoms to Nanoclusters and Nanoparticles, *Chem. Rev.*, 2018, **118**, 4981–5079.
2 D. Astruc, Introduction: Nanoparticles in Catalysis, *Chem. Rev.*, 2020, **120**, 461–463.

3 A. T. Bell, The Impact of Nanoscience on Heterogeneous Catalysis, *Science*, 2003, **299**, 1688–1691.
4 J. Qiao, Y. Liu, F. Hong and J. Zhang, A Review of Catalysts for the Electroreduction of Carbon Dioxide to Produce Low-Carbon Fuels, *Chem. Soc. Rev.*, 2014, **43**, 631–675.
5 W.-H. Wang, Y. Himeda, J. T. Muckerman, G. F. Manbeck and E. Fujita, CO_2 Hydrogenation to Formate and Methanol as an Alternative to Photo- and Electrochemical CO_2 Reduction, *Chem. Rev.*, 2015, **115**, 12936–12973.
6 P. De Luna, C. Hahn, D. Higgins, S. A. Jaffer, T. F. Jaramillo and E. H. Sargent, What Would It Take for Renewably Powered Electrosynthesis to Displace Petrochemical Processes?, *Science*, 2019, **364**, eaav3506.
7 S. Zhao, R. Jin and R. Jin, Opportunities and Challenges in CO_2 Reduction by Gold- and Silver-Based Electrocatalysts: From Bulk Metals to Nanoparticles and Atomically Precise Nanoclusters, *ACS Energy Lett.*, 2018, **3**, 452–462.
8 T. Ishida, T. Murayama, A. Taketoshi and M. Haruta, Importance of Size and Contact Structure of Gold Nanoparticles for the Genesis of Unique Catalytic Processes, *Chem. Rev.*, 2020, **120**, 464–525.
9 S. Panigrahi, S. Basu, S. Praharaj, S. Pande, S. Jana, A. Pal, S. K. Ghosh and T. Pal, Synthesis and Size-Selective Catalysis by Supported Gold Nanoparticles: Study on Heterogeneous and Homogeneous Catalytic Process, *J. Phys. Chem. C*, 2007, **111**, 4596–4605.
10 X. Zhou, W. Xu, G. Liu, D. Panda and P. Chen, Size-Dependent Catalytic Activity and Dynamics of Gold Nanoparticles at the Single-Molecule Level, *J. Am. Chem. Soc.*, 2010, **132**, 138–146.
11 R. Si and M. Flytzani-Stephanopoulos, Shape and Crystal-Plane Effects of Nanoscale Ceria on the Activity of Au–CeO_2 Catalysts for the Water–Gas Shift Reaction, *Angew. Chem., Int. Ed.*, 2008, **47**, 2884–2887.
12 M. Jin, H. Zhang, Z. Xie and Y. Xia, Palladium Nanocrystals Enclosed by {100} and {111} Facets in Controlled Proportions and Their Catalytic Activities for Formic Acid Oxidation, *Energy Environ. Sci.*, 2012, **5**, 6352–6357.
13 L. M. Rossi, J. L. Fiorio, M. A. S. Garcia and C. P. Ferraz, The Role and Fate of Capping Ligands in Colloidally Prepared Metal Nanoparticle Catalysts, *Dalton Trans.*, 2018, **47**, 5889–5915.
14 L. Lu, S. Zou and B. Fang, The Critical Impacts of Ligands on Heterogeneous Nanocatalysis: A Review, *ACS Catal.*, 2021, **11**, 6020–6058.
15 S. Schauermann, N. Nilius, S. Shaikhutdinov and H.-J. Freund, Nanoparticles for Heterogeneous Catalysis: New Mechanistic Insights, *Acc. Chem. Res.*, 2013, **46**, 1673–1681.
16 C. Xie, Z. Niu, D. Kim, M. Li and P. Yang, Surface and Interface Control in Nanoparticle Catalysis, *Chem. Rev.*, 2020, **120**, 1184–1249.
17 Y. Li and R. Jin, Seeing Ligands on Nanoclusters and in Their Assemblies by X-Ray Crystallography: Atomically Precise Nanochemistry and Beyond, *J. Am. Chem. Soc.*, 2020, **142**, 13627–13644.
18 Z. Cao, D. Kim, D. Hong, Y. Yu, J. Xu, S. Lin, X. Wen, E. M. Nichols, K. Jeong, J. A. Reimer, P. Yang and C. J. Chang, A Molecular Surface Functionalization Approach to Tuning Nanoparticle Electrocatalysts for Carbon Dioxide Reduction, *J. Am. Chem. Soc.*, 2016, **138**, 8120–8125.
19 Z. Cao, S. B. Zacate, X. Sun, J. Liu, E. M. Hale, W. P. Carson, S. B. Tyndall, J. Xu, X. Liu, X. Liu, C. Song, J. Luo, M.-J. Cheng, X. Wen and W. Liu, Tuning Gold Nanoparticles with Chelating Ligands for Highly Efficient Electrocatalytic CO_2 Reduction, *Angew. Chem., Int. Ed.*, 2018, **57**, 12675–12679.
20 G. Li and R. Jin, Atomically Precise Gold Nanoclusters as New Model Catalysts, *Acc. Chem. Res.*, 2013, **46**, 1749–1758.
21 Y. Du, H. Sheng, D. Astruc and M. Zhu, Atomically Precise Noble Metal Nanoclusters as Efficient Catalysts: A Bridge between Structure and Properties, *Chem. Rev.*, 2020, **120**, 526–622.
22 R. Jin, G. Li, S. Sharma, Y. Li and X. Du, Toward Active-Site Tailoring in Heterogeneous Catalysis by Atomically Precise Metal Nanoclusters with Crystallographic Structures, *Chem. Rev.*, 2021, **121**, 567–648.
23 Y. Li, T. Higaki, X. Du and R. Jin, Chirality and Surface Bonding Correlation in Atomically Precise Metal Nanoclusters, *Adv. Mater.*, 2020, 1905488.
24 D. R. Kauffman, D. Alfonso, C. Matranga, H. Qian and R. Jin, Experimental and Computational Investigation of Au_{25} Clusters and CO_2: A Unique Interaction and Enhanced Electrocatalytic Activity, *J. Am. Chem. Soc.*, 2012, **134**, 10237–10243.
25 Z.-H. Gao, K. Wei, T. Wu, J. Dong, D. Jiang, S. Sun and L.-S. Wang, A Heteroleptic Gold Hydride Nanocluster for Efficient and Selective Electrocatalytic Reduction of CO_2 to CO, *J. Am. Chem. Soc.*, 2022, **144**, 5258–5262.
26 V. K. Kulkarni, B. N. Khiarak, S. Takano, S. Malola, E. L. Albright, T. I. Levchenko, M. D. Aloisio, C.-T. Dinh, T. Tsukuda, H. Häkkinen and C. M. Crudden, N-Heterocyclic Carbene-Stabilized Hydrido Au_{24} Nanoclusters: Synthesis, Structure, and Electrocatalytic Reduction of CO_2, *J. Am. Chem. Soc.*, 2022, **144**, 9000–9006.
27 S.-F. Yuan, R.-L. He, X.-S. Han, J.-Q. Wang, Z.-J. Guan and Q.-M. Wang, Robust Gold Nanocluster Protected with Amidinates for Electrocatalytic CO_2 Reduction, *Angew. Chem., Int. Ed.*, 2021, **60**, 14345–14349.
28 L. Qin, F. Sun, X. Ma, G. Ma, Y. Tang, L. Wang, Q. Tang, R. Jin and Z. Tang, Homoleptic Alkynyl-Protected Ag_{15} Nanocluster with Atomic Precision: Structural Analysis and Electrocatalytic Performance toward CO_2 Reduction, *Angew. Chem., Int. Ed.*, 2021, **60**, 26136–26141.
29 P. Maity, H. Tsunoyama, M. Yamauchi, S. Xie and T. Tsukuda, Organogold Clusters Protected by Phenylacetylene, *J. Am. Chem. Soc.*, 2011, **133**, 20123–20125.
30 M. G. Taylor and G. Mpourmpakis, Thermodynamic Stability of Ligand-Protected Metal Nanoclusters, *Nat. Commun.*, 2017, **8**, 15988.

31 B. Zhang, J. Chen, Y. Cao, O. J. H. Chai and J. Xie, Ligand Design in Ligand-Protected Gold Nanoclusters, *Small*, 2021, **17**, 2004381.
32 S. Li, X. Du, Z. Liu, Y. Li, Y. Shao and R. Jin, Size Effects of Atomically Precise Gold Nanoclusters in Catalysis, *Precis. Chem.*, 2023, **1**, 14–28.
33 H. Seong, V. Efremov, G. Park, H. Kim, J. S. Yoo and D. Lee, Atomically Precise Gold Nanoclusters as Model Catalysts for Identifying Active Sites for Electroreduction of CO_2, *Angew. Chem., Int. Ed.*, 2021, **60**, 14563–14570.
34 S. Li, A. V. Nagarajan, X. Du, Y. Li, Z. Liu, D. R. Kauffman, G. Mpourmpakis and R. Jin, Dissecting Critical Factors for Electrochemical CO_2 Reduction on Atomically Precise Au Nanoclusters, *Angew. Chem., Int. Ed.*, 2022, **61**, e202211771.
35 Y. Li, H. K. Kim, R. D. McGillicuddy, S.-L. Zheng, K. J. Anderton, G. J. Stec, J. Lee, D. Cui and J. A. Mason, A Double Open-Shelled Au_{43} Nanocluster with Increased Catalytic Activity and Stability, *J. Am. Chem. Soc.*, 2023, **145**, 9304–9312.
36 J. Xu, L. Xiong, X. Cai, S. Tang, A. Tang, X. Liu, Y. Pei and Y. Zhu, Evolution from Superatomic $Au_{24}Ag_{20}$ Monomers into Molecular-like $Au_{43}Ag_{38}$ Dimeric Nanoclusters, *Chem. Sci.*, 2022, **13**, 2778–2782.
37 Y. Tang, F. Sun, X. Ma, L. Qin, G. Ma, Q. Tang and Z. Tang, Alkynyl and Halogen Co-Protected $(AuAg)_{44}$ Nanoclusters: A Comparative Study on Their Optical Absorbance, Structure, and Hydrogen Evolution Performance, *Dalton Trans.*, 2022, **51**, 7845–7850.
38 S. Takano, S. Hasegawa, M. Suyama and T. Tsukuda, Hydride Doping of Chemically Modified Gold-Based Superatoms, *Acc. Chem. Res.*, 2018, **51**, 3074–3083.
39 S. Takano, S. Ito and T. Tsukuda, Efficient and Selective Conversion of Phosphine-Protected $(MAu_8)^{2+}$ (M = Pd, Pt) Superatoms to Thiolate-Protected $(MAu_{12})^{6+}$ or Alkynyl-Protected $(MAu_{12})^{4+}$ Superatoms *via* Hydride Doping, *J. Am. Chem. Soc.*, 2019, **141**, 15994–16002.
40 F. Wen, U. Englert, B. S. Gutrath and U. Simon, Crystal Structure, Electrochemical and Optical Properties of $[Au_9(PPh3)_8](NO_3)_3$, *Eur. J. Inorg. Chem.*, 2008, 106–111.
41 N. Yan, N. Xia, L. Liao, M. Zhu, F. Jin, R. Jin and Z. Wu, Unraveling the Long-Pursued Au_{144} Structure by X-Ray Crystallography, *Sci. Adv.*, 2018, **4**, eaat7259.
42 Y. Li, R. Juarez-Mosqueda, Y. Song, Y. Zhang, J. Chai, G. Mpourmpakis and R. Jin, Ligand Exchange on $Au_{38}(SR)_{24}$: Substituent Site Effects of Aromatic Thiols, *Nanoscale*, 2020, **12**, 9423–9429.
43 L. G. AbdulHalim, M. S. Bootharaju, Q. Tang, S. Del Gobbo, R. G. AbdulHalim, M. Eddaoudi, D.-e. Jiang and O. M. Bakr, $Ag_{29}(BDT)_{12}(TPP)_4$: A Tetravalent Nanocluster, *J. Am. Chem. Soc.*, 2015, **137**, 11970–11975.
44 Y. Song, Y. Li, M. Zhou, X. Liu, H. Li, H. Wang, Y. Shen, M. Zhu and R. Jin, Ultrabright Au@Cu_{14} Nanoclusters: 71.3% Phosphorescence Quantum Yield in Non-Degassed Solution at Room Temperature, *Sci. Adv.*, 2021, **7**, eabd2091.
45 Y. Li, T.-Y. Luo, M. Zhou, Y. Song, N. L. Rosi and R. Jin, A Correlated Series of Au/Ag Nanoclusters Revealing the Evolutionary Patterns of Asymmetric Ag Doping, *J. Am. Chem. Soc.*, 2018, **140**, 14235–14243.
46 Y. Li, M. Zhou, Y. Song, T. Higaki, H. Wang and R. Jin, Double-Helical Assembly of Heterodimeric Nanoclusters into Supercrystals, *Nature*, 2021, **594**, 380–384.
47 M. J. Alhilaly, R.-W. Huang, R. Naphade, B. Alamer, M. N. Hedhili, A.-H. Emwas, P. Maity, J. Yin, A. Shkurenko, O. F. Mohammed, M. Eddaoudi and O. M. Bakr, Assembly of Atomically Precise Silver Nanoclusters into Nanocluster-Based Frameworks, *J. Am. Chem. Soc.*, 2019, **141**, 9585–9592.
48 Y. Li, M. J. Cowan, M. Zhou, T.-Y. Luo, Y. Song, H. Wang, N. L. Rosi, G. Mpourmpakis and R. Jin, Atom-by-Atom Evolution of the Same Ligand-Protected Au_{21}, Au_{22}, $Au_{22}Cd_1$, and Au_{24} Nanocluster Series, *J. Am. Chem. Soc.*, 2020, **142**, 20426–20433.
49 Y. Li, S. Li, A. V. Nagarajan, Z. Liu, S. Nevins, Y. Song, G. Mpourmpakis and R. Jin, Hydrogen Evolution Electrocatalyst Design: Turning Inert Gold into Active Catalyst by Atomically Precise Nanochemistry, *J. Am. Chem. Soc.*, 2021, **143**, 11102–11108.
50 C. Kim, H. S. Jeon, T. Eom, M. S. Jee, H. Kim, C. M. Friend, B. K. Min and Y. J. Hwang, Achieving Selective and Efficient Electrocatalytic Activity for CO_2 Reduction Using Immobilized Silver Nanoparticles, *J. Am. Chem. Soc.*, 2015, **137**, 13844–13850.
51 S. Liu, H. Tao, L. Zeng, Q. Liu, Z. Xu, Q. Liu and J.-L. Luo, Shape-Dependent Electrocatalytic Reduction of CO_2 to CO on Triangular Silver Nanoplates, *J. Am. Chem. Soc.*, 2017, **139**, 2160–2163.
52 C. Vogt and B. M. Weckhuysen, The Concept of Active Site in Heterogeneous Catalysis, *Nat. Rev. Chem*, 2022, **6**, 89–111.
53 J. K. Nørskov, T. Bligaard, B. Hvolbæk, F. Abild-Pedersen, I. Chorkendorff and C. H. Christensen, The Nature of the Active Site in Heterogeneous Metal Catalysis, *Chem. Soc. Rev.*, 2008, **37**, 2163–2171.
54 G. Kumar, L. Tibbitts, J. Newell, B. Panthi, A. Mukhopadhyay, R. M. Rioux, C. J. Pursell, M. Janik and B. D. Chandler, Evaluating Differences in the Active-Site Electronics of Supported Au Nanoparticle Catalysts Using Hammett and DFT Studies, *Nat. Chem.*, 2018, **10**, 268–274.
55 T. Higaki, Y. Li, S. Zhao, Q. Li, S. Li, X.-S. Du, S. Yang, J. Chai and R. Jin, Atomically Tailored Gold Nanoclusters for Catalytic Application, *Angew. Chem., Int. Ed.*, 2019, **58**, 8291–8302.
56 R. T. Yang, *Adsorbents: Fundamentals and Applications*, John Wiley & Sons, Inc., Hoboken: New Jersey, 2003.
57 G. Deng, J. Kim, M. S. Bootharaju, F. Sun, K. Lee, Q. Tang, Y. J. Hwang and T. Hyeon, Body-Centered-Cubic-Kernelled $Ag_{15}Cu_6$ Nanocluster with Alkynyl Protection: Synthesis, Total Structure, and CO_2 Electroreduction, *J. Am. Chem. Soc.*, 2022, **145**, 3401–3407.
58 S. Li, A. V. Nagarajan, Y. Li, D. R. Kauffman, G. Mpourmpakis and R. Jin, The Role of Ligands in Atomically Precise Nanocluster-Catalyzed CO_2 Electrochemical Reduction, *Nanoscale*, 2021, **13**, 2333–2337.
59 X. Liu, E. Wang, M. Zhou, Y. Wan, Y. Zhang, H. Liu, Y. Zhao, J. Li, Y. Gao and Y. Zhu, Asymmetrically Doping a Platinum

Atom into a Au_{38} Nanocluster for Changing the Electron Configuration and Reactivity in Electrocatalysis, *Angew. Chem., Int. Ed.*, 2022, **61**, e202207685.

60 Z.-J. Guan, F. Hu, J.-J. Li, Z.-R. Wen, Y.-M. Lin and Q.-M. Wang, Isomerization in Alkynyl-Protected Gold Nanoclusters, *J. Am. Chem. Soc.*, 2020, **142**, 2995–3001.

61 X.-K. Wan, Z.-J. Guan and Q.-M. Wang, Homoleptic Alkynyl-Protected Gold Nanoclusters: $Au_{44}(PhC{\equiv}C)_{28}$ and $Au_{36}(PhC{\equiv}C)_{24}$, *Angew. Chem., Int. Ed.*, 2017, **56**, 11494–11497.